Dalton Transactions

Crystal structure, bonding and electronic structure of *α*- and *β*-Ir_2B_{3-x} compounds

Journal:	*Dalton Transactions*
Manuscript ID	DT-ART-07-2024-002095.R1
Article Type:	Paper
Date Submitted by the Author:	20-Aug-2024
Complete List of Authors:	Sologub, Oksana; TU Wien, Institute of Solid State Physics Salamakha, Leonid; TU Wien, Institute of Solid State Physics Stöger, Berthold; TU Wien, X-Ray Center Mori, Takao; National Institute for Materials Science, International Center for Materials Nanoarchitectonics (WPI-MANA) Barisic, Neven; TU Wien, Institute of Solid State Physics Rogl, Peter; University of Vienna, Institute of Materials Chemistry Michor, Herwig; TU Wien, Institute of Solid State Physics Bauer, Ernst; Technische Universitat Wien, Institute of Solid Sate Physics

Crystal structure, bonding and electronic structure of α- and β-Ir_2B_{3-x} compounds

Oksana Sologub[1,*], Leonid P. Salamakha[1,5], Berthold Stöger[2], Takao Mori[3], Neven Barisic[1,6], Peter F. Rogl[4], Herwig Michor[1], Ernst Bauer[1]

[1]Institute of Solid State Physics, TU Wien, A-1040 Vienna, Austria

[2]X-Ray Centre, TU Wien, A-1060 Vienna, Austria

[3]National Institute for Materials Science (NIMS), Research Center for Materials Nanoarchitectonics (MANA), Tsukuba, Japan

[4]Institute of Materials Chemistry, University of Vienna, A-1090 Vienna, Austria

[5]Department of Physics of Metals, Faculty of Physics, I. Franko L'viv National University, 79005, L'viv, Ukraine

[6]Department of Physics, Faculty of Science, University of Zagreb, Croatia

ABSTRACT

The binary boron rich compounds α-Ir_2B_{3-x} and β-Ir_2B_{3-x}, formerly denoted as α- and β-Ir_4B_5, were synthesized both via arc melting followed by annealing at 800 °C (900 °C) and high-temperature thermal treatment of mixtures of the elements. X-ray structure analysis of α-Ir_2B_{3-x} was performed on single crystal (space group *C*2/*m*, *a*=10.5515(11) Å, *b*=2.8842(3) Å, *c*=6.0965(7) Å, β =91.121(9)º). The orthorhombic structure of β-Ir_2B_{3-x} was confirmed by X-ray powder diffraction (space group *Pnma*; *a*=10.7519(3) Å, *b*=2.83193(7) Å, *c*=6.0293(1) Å). The α-Ir_2B_{3-x} structure exhibits ordered arrangements of iridium atoms. The structure is built of corrugated layers of boron hexagons (interlinked via external B-B bonds) alternated with two corrugated layers of iridium along the *c*-direction; an additional boron (Oc. 0.46(7)) is located between iridium layers in Ir_6 trigonal prisms. The boron partial structure in β-Ir_2B_{3-x} is composed of ribbons built up of slightly corrugated quadrilaterial units running along *b*-direction in the channels formed by 8 iridium atoms each. DFT calculations revealed a number of bands crossing the Fermi level, predicting metallic behaviors of the two compounds. β-Ir_2B_{3-x} is characterized by a pseudogap around the Fermi level and a smaller eDOS of 0.6405 states/eV*f.u. at the Fermi level, as compared to the α-Ir_2B_{3-x} value of 1.405 states/eV*f.u. The calculated electron localization functions revealed strong covalent bonds between boron atoms in the core part of the B_6 hexagons, metallic B-B bonds within the quadrilaterial boron partial structure and mixed covalent and metallic interaction between iridium and boron atoms.

Structural relationships of α-Ir_2B_{3-x} and β-Ir_2B_{3-x} with ReB_2-type as well as the common structural features with layered binary borides with CrB-type related structures have been discussed.

Keywords: Iridium Borides; Transition Metal Borides; Crystal Structure; Bonding Analysis; Density Functional Theory Calculations

* Corresponding author
E-mail address: oksana.sologub@univie.ac.at.

1. INTRODUCTION

Metal compounds with boron display an extensive diversity of crystal structures and attractive mechanical, electronic, optical, refractory and other properties.[1-9] On increasing of boron content in borides, the boron structural units evolve from isolated B atoms via isolated/condensed chains and 2D boron networks to 3D boron atom frameworks.

Transition metal borides with a B/M ratio ≥ 2 are often considered as potential candidates for hard, incompressible and refractory materials. In the crystal structure of diborides, the layers of boron hexagons alternate with metallic layers; the boron sheets can be flat (AlB_2 structure) or corrugated ("chair" conformation in ReB_2 and "boat" conformation in RuB_2).[10-12] A directional covalent bonding coming from boron sheets (resisting the shear stress) in combination with high electron density at the Fermi level (E_F) introduced by transition metal (making borides incompressible) are considered as two essential parameters for hardness of this class of materials.[13-18] Numerous theoretical studies elucidated bonding features leading to the increase in hardness with increase of B content, such as the occurrence of strong B–B covalent bonds with short bond lengths and the disappearance of ductile M-M metallic bonds along some specific axial directions,[16] strong covalent bonding of B-hexagon and enhanced directional covalent M-B bonding.[17]

At a B/M ratio equal/ slightly higher than 1, the boron atoms are arranged in zig-zag chains, condensed double chains (Ta_3B_4-type[19]), triple chains (V_2B_3-type[20]) or a combination of single and double chains (V_5B_6-type[21]); coordination polyhedra of boron atoms are M_6 trigonal prisms. The face-sharing BM_6 trigonal prisms constitute the metal boride subunits of the MAB phases, a group of atomically laminated, transition metal borides.[22-28] MAB phases are usually composed of an early transition metal (M), metals from groups 13 and 14 of the periodic table (A), and boron (B) and contain stacked M–B blocks, interleaved by A atom layers or intermetallic complexes of A layers. These layered materials combine both metallic (ductility, machinability) and ceramic (refractory properties and oxidation resistance) attributes and are extensively investigated due to their excellent mechanical and tribological properties.[29-30] Various MAB-phase compositions make them promising candidates for the establishment of tailored tribo-films for the specific matrix material or tribo-couple.[29-30] MAB phases possess metallic M-A bonds, being weaker than the rest of the bonds (M-B and B-B bonds exhibiting mixed covalent/metal/ionic characteristics) thus enabling their reactive liquid-phase delamination into their corresponding 2D counterparts, MBenes, composed of M and B.[30] MBenes are expected to have high performance in fields of energy storage, catalysis, biosensors, and biomedical devices, as well as tribology and lubrication.[29-31] However, despite different approaches are pursued, synthesis of MBenes is still at an early stage. Moreover, elemental range for A component in MAB structures is limited to representatives, found in traditional ternary phases,[21] besides few new MAB phases reported more recently.[24-28,32-34] In general, a future challenge in the

field of MAB phases is the extension of the family towards new elemental compositions and unconventional chemical formulae realized via experimental synthesis, structural and bonding analysis of layered structures.[29,30]

No unambiguous data on crystal structures and compositional ranges of binary iridium borides have been available for several decades[12,35] until the report of Zeiringer et al. (2015)[36] on the constitution of the Ir-B phase diagram. The boron-rich compound obtained by arc-melting was denoted as Ir_4B_5 (according to its nominal composition elucidated from single crystal X-ray diffraction) and revealed a good agreement with the disordered structure model suggested hitherto.[35] Later on, the new iridium borides IrB_2 (ReB_2-type) and orthorhombic IrB have been obtained from mechanochemical synthesis.[37] More recent experimental work on the synthesis of the Ir_2B_{3-x} phase under high-pressure/high-temperature conditions revealed the formation of a new orthorhombic structure (denoted as β-Ir_4B_5; space group *Pnma*).[38] In contrast to thin films of $IrB_{1.35}$, which exhibited enhanced hardness,[39] the hardness of the orthorhombic compound was found to be significantly smaller (H_V at 9.8 N = 15.8(1.2) GPa to H_V at 0.49 N = 22.6(2.8) GPa).[38] A series of crystalline IrB_x phases within x=1.5-6 has been theoretically investigated for formation of stable at ambient or high pressures structures; the predicted structures exhibited a variety of boron networks (zigzag chains, triangles, rhomboids).[40] The concentration range with B/Ir ratio ≥8 has been searched for the 2D-IrB_x systems both theoretically and experimentally;[41,42] a planar hypervalent IrB_9 ring has been synthesized[42] and showed promise as a precursor of synthesizing 2D IrB_x.

In general, layered boron-rich iridium borides and their alloys are supposed to possess characteristics required for the design of hard and/or incompressible materials, as well as to exhibit high melting points, high level of mechanical properties, and good oxidation and corrosion resistance.[43] On the other hand, iridium is predicted to form MAB phases acting as A element.[29,30] Since the layered phases are potentially sensitive to lattice defects and unwanted phase transitions, the exploration of electronic structure and bonding in synergy with experimental studies on synthesis and crystal structure of boron rich iridium borides is of great importance for expanding the field of new layered materials. In the course of our investigations of the iridium boron rich borides, we have observed the formation of two variants of Ir_2B_{3-x} with nominal composition ~$Ir_{44.5}B_{55.5}$. As there still remained an open question concerning the atom ordering in the crystal structure of the monoclinic α-Ir_2B_{3-x} (formerly denoted as Ir_4B_5), in the present work we have carried out the synthesis of this compound in single phase condition, elucidation of its crystal structure, characterization of bonding and electronic structure. We also synthesized the orthorhombic β-Ir_2B_{3-x} phase at ambient conditions (synthesized hitherto at high pressure/high temperature)[38] and explored the underlying electronic structure in terms of density of states, band structures and electron localization function distribution.

2. EXPERIMENTAL

2.1. Synthesis and powder X-ray diffraction

Alloys were prepared from ingots of thoroughly re-melted pieces of iridium sponge and pieces of pre-synthesized master alloy $IrB_{4.5}$ (B, 99.4 mass%, ChemPur, Germany; remelted Ir sponge, 99.9 mass%, Ögussa, Austria) by repeated arc melting under argon. The arc-melted buttons were wrapped in tantalum foil and vacuum-sealed in a quartz tube for annealing at 800 °C or 900 °C for 240 hours. For high temperature synthesis in a radio frequency induction furnace, the proper weight ratios of amorphous boron (3N, SB-Boron Inc., USA) and iridium powder (99.9 mass%, Sigma-Aldrich, USA) were well mixed in mortar and compacted by cold iso-static pressing into cylindrical bars applying a pressure of 300 MPa. The compacted rod was placed in a crucible made from sintered BN which was inserted into a graphite susceptor. The reaction process was performed under dynamic vacuum at a predetermined temperature of about 1700 °C for 6 h; afterwards the setup was cooled down in 1 h to room temperature. After synthesis, the samples were powderized in a c-BN mortar, compacted in a steel die without lubricant and annealed in a BN crucible for 4 h under dynamic vacuum at 1500 °C. The obtained sample was subjected to chemical analysis which was performed by inductively coupled plasma atomic emission spectroscopy (ICP-AES). No traces of nitrogen or carbon impurities have been detected. Lattice parameters were determined by least squares refinements of room temperature X-ray powder diffraction (XRD) data obtained from a Guinier-Huber image plate system with monochromatic Cu $K\alpha_1$ radiation ($8^\circ<2\theta<100^\circ$) and a standard high-resolution powder X-ray diffractometer (R-2000, Rigaku Co.) with Cu$K\alpha$ radiation. XRD Rietveld refinements were performed with the program FULLPROF[44] with the use of its internal tables for atom scattering factors.

2.2. Single crystal X-ray diffraction

The crystal structure of α-Ir_2B_{3-x} was elucidated from X-ray diffraction intensity data of a single crystal (45μm×55μm×53μm) which was isolated via mechanical fragmentation of the $Ir_{45}B_{55}$ sample annealed at 800ºC. The crystal was measured on a four-circle STOE Stadivari diffractometer equipped with a Eiger CdTe hybrid photon counting detector (Euler geometry, Mo Kα radiation). Orientation matrices and unit cell parameters were derived with the help of the diffractometers' software; the data were scaled using the multi-scan approach implemented in LANA.[45] Space group determination, structure solution and refinement were performed employing WinGX program package.[46-49] Further details concerning the single crystal X-ray diffraction experiments are summarized in Table 1.

2.3. Electronic structure calculations and chemical bonding analysis

Band structure (electron dispersion) and density of states (eDOS) calculations were performed within the DFT framework using the Quantum ESPRESSO 6.7 package[50] on structural models α-Ir_2B_{3-x} and β-Ir_2B_{3-x} which assume a full occupation of B3 (4*i* (*x*,0,*z*) *x*=0.740(4), *z*=0.0565) and B3 (4*c* (*x*, ¼,*z*) *x*=0.008, *z*=0.557) atomic position for the first and second compound, respectively. Correlation and exchange effects of the electrons were handled utilizing the generalized gradient approximation (GGA) of Perdew, Burke, and Ernzerhof, revised for solids (PBEsol).[51] Electron-ion interactions were treated using both fully relativistic and pseudo-relativistic projector augmented wave (PAW[52,53]) potentials constructed according to the code supplied by the PSLibrary (version 1.0.0).[54] For iridium, the 4*f*-, 5*s*- and 5*p*- were considered as valence states. The electron wave functions were expanded into plane waves with a kinetic energy cutoff of 71 Ry. For the charge density, a kinetic energy cutoff of 446 Ry was used. The unit cell parameters and atomic positions of α-Ir_2B_{3-x} and β-Ir_2B_{3-x} were relaxed using the Broyden-Fletcher-Goldfarb-Shanno (BFGS) algorithm. A 4x15x7 k-point mesh constructed using the Monkhorst–Pack method[55] that guarantees a less than 0.15 $Å^{-1}$ spacing between the k-points was used during the relaxation procedure of both models. A denser grid of 8x30x14 was used for the calculation of the electronic densities of states (DOS). The convergence threshold for self-consistent-field iteration was set at 10^{-9} eV. ELF distribution was analyzed and visualized using the VESTA v.3.5.8 software.[56]

3. RESULTS

3.1. Crystal structures of α-Ir_2B_{3-x} (x=0.54)

X-ray single crystal diffraction data were indexed in a monoclinic base-centered lattice (*a*=10.5515(11) Å, *b*=2.8842(3) Å, *c*=6.0965(7) Å, β=91.121(9)°). Systematic extinctions in the single crystal X-ray data were consistent with three possible space group types: *C*2/*m* (no. 12), *Cm* (no. 8) and *C*2 (no. 5), out of which the highest symmetric one, *C*2/*m*, was chosen for further structure analysis. Direct methods delivered a structure solution with two 4*i* atom positions of iridium. Two atom sites of B (4*i*) were found from difference Fourier maps after subsequent refinement of iridium atoms. The refinements with free site occupation factors showed full occupation for all four atom positions (two iridium and two boron sites). B3 was found on the 4*i* site (*x*,0,*z*; *x*=0.740, *z*=0.0565) from difference Fourier map, however, the low value of electron density (~6 e−/$Å^3$) hinted towards a fractional population which was further refined to about 46% B. The large difference in the scattering power between iridium and boron imposes difficulties in defining the positional parameter at low boron population level, therefore the positional parameter (i.e. *z*), occupation and ADP for B3 in this structure were alternately constrained to a pre-refined value at each consequent cycle of refinement until reaching convergence with anisotropic ADP's for Ir atoms and isotropic ADP's for B atoms at

a reliability factor value as low as R_F^2=0.0372 yielding residual electron density peaks +3.87 e-/Å^3 and -3.76 e-/Å^3 at 0.75 Å from Ir2 and 0.56 Å from Ir1 respectively. We should note, that similarly to platinum borides, e.g. $Pt_{12}CuB_{6-y}$, $Pt_{12}(Al_{1-x}Pt_x)B_{6-y}$,[57] in the case of dismissing positional parameter constraints of B3, the atom was drifting along *z* (into *z*=0.036(7)) until reaching the vicinity (d_{B3-B3}=1.53(2) Å) of a symmetry equivalent boron. This short distance between boron atoms would exclude their simultaneous presence; besides, the partial occupancy of boron atom position supports the understanding that only an average B3 substructure has been determined. The refinements in the space group types with lower symmetry (*Cm*, *C*2) yielded inferior results. The relevant crystallographic data are given in Table 1; for bond lengths values see Table 2. X-ray powder diffraction intensities collected from the polycrystalline alloy with nominal composition $Ir_{45}B_{55}$ were in good agreement with the intensities calculated from the structural model obtained from single crystal as inferred from Rietveld refinement (Figure 1).

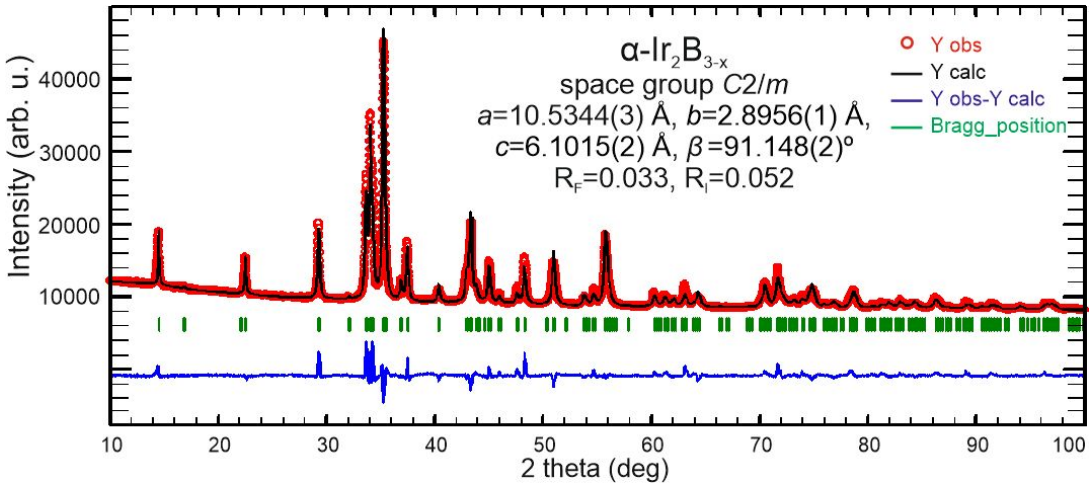

Figure 1. X-ray powder diffraction pattern of $Ir_{45}B_{55}$ annealed at 800 ºC.

No features prompting the displacement of the metal atoms from the mirror plane, reported by Lundstrom et al.[35] and Zeiringer et al. (2015)[36] (and supporting "model 2"[36]) have been observed in our single crystal X-ray diffraction study. Two iridium atoms in two 4*i* positions were perfectly refined yielding spherical ADPs (Table 1, Figure 2). The finally refined formula of the crystal is $Ir_2B_{2.46}$, which is of a slightly lower boron content than that proposed by Aronsson (1963)[12] and Lundstrom (1973)[35], however is very close to that, obtained in "model 1" by Zeiringer et al. (2015)[36]. The Ir1 and Ir2 have 8 and 7 close iridium neighbors respectively within the same iridium boride layer; Ir-Ir distances range from 2.6671(9) Å to 3.0876(9) Å (Table 2) and are similar to the iridium−iridium distances in other borides.[36,58,59] The Ir-B distances are 2.09(3) Å - 2.36(2) Å within the trigonal prisms and 2.11(2) Å - 2.20(2) Å between metal and boride layers; the shortest among them (e.g. 2.09(3) Å, 2.13(3) Å, etc) are slightly shorter than the sum of the covalent radii of B and

Ir, however are similar to those reported earlier for iridium borides.[36,58,59] The metal atoms built columns (running in *b* direction) of face-sharing Ir_6 trigonal prims half-filled with boron. As the B3 position inside the B6 trigonal prisms is almost 50% statistically occupied, some chain fragments with B3-B3 distance 1.614(8) Å may exist. The trigonal-prismatic columns interlink via Ir-Ir bonds. The B1 and B2 form a boron layer of puckered hexagons. The B-B distances within hexagons are 1.96(2) Å for B1-B2 and 1.93(3) Å for B2-B2. The boron hexagons are interconnected via rather long B1-B1 contacts of 2.13(2) Å leading to formation of layers of puckered hexagons and distorted squares (Figure 2, Figure 7). B1 is coordinated by four boron atoms and 4 iridium atoms (iridium tetrahedron with four additional boron atoms). B2 has three close boron neighbors and four iridium neighbors leading to 7-fold coordination (iridium triangular-based pyramid with three additional B atoms).

Table 1. Structure refinement details from single crystal XRD

	α-Ir_2B_{3-x} (x=0.54)
Nominal composition	$Ir_{44.8}B_{55.2}$
Space group	*C*2/*m*; No. 12
Structure type	Ir_2B_{3-x}
Formula from refinement	$Ir_2B_{2.46}$
Range for data collection	$3.34° < \theta < 34.42°$
a (Å)	10.5515(11)
b (Å)	2.8842(3)
c (Å)	6.0965(7)
β (deg)	91.121(9)
Z	4
Reflections in refinement	417 $F_o > 4\sigma(F_o)$ of 3391
Mosaicity	<0.4
Number of variables	23
R_F^2	0.0372
GOF	1.202
Extinction (Zachariasen)	0.0012(4)
Ir1 in 4*i* (*x*,0,*z*); Occ.	*x*=0.09953(6), *z*=0.1382(1); 1.00
U_{11}[a], U_{22}, U_{33}, U_{12}	0.0098(3), 0.0100(3), 0.0091(3), -0.0017(2)
Ir2 in 4*i* (*x*,0,*z*); Occ.	*x*=0.35744(6), *z*=0.2883(1); 1.00
U_{11}, U_{22}, U_{33}, U_{13}	0.0096(3), 0.0097(3), 0.0088(3), -0.0010(2)
B1 in 4*i* (*x*,0,*z*); Occ.	*x*=0.179(2), *z*=0.459(3); 1.00
U_{iso}[b]	0.011(3)
B2 in 4*i* (*x*,0,*z*); Occ.	*x*=0.560(2), *z*=0.383(3); 1.00
U_{iso}	0.011(3)
B3 in 4*i* (*x*,0,*z*); Occ.	*x*=0.740(4), *z*=0.0565[c]; 0.46(7)
U_{iso}	0.012(6)
Residual density; max;min ($e^-/Å^3$)	+3.87; -3.76

[a]anisotropic (U_{ij}) displacement parameters in $Å^2$, $U_{23}=U_{12}=0$; [b]isotropic (U_{iso}) atomic displacement parameters in $Å^2$; [c]fixed parameter.

Table 2. Interatomic distances in α-Ir_2B_{3-x} (x=0.54) (Å) [a]

Ir1 –	B3	2.09(3)	B1 – 2	B2	1.96(2)
	B1	2.11(2)		Ir1	2.11(2)
	2 B2	2.12(1)		2 B1	2.13(2)
	2 B3	2.13(3)		2 Ir2	2.15(1)
	Ir1	2.6671(9)		Ir2	2.17(2)
	Ir2	2.8540(9)	B2 –	B2	1.93(3)
	2 Ir1	2.8842(3)		2 B1	1.96(2)
	2 Ir2	3.0156(8)		2 Ir1	2.12(1)
	2 Ir2	3.0876(9)		Ir2	2.17(2)
Ir2 – 2	B1	2.15(1)		Ir2	2.20(2)
	B2	2.17(2)	B3 – 2	B3	1.614(8)
	B1	2.17(2)		Ir1	2.09(3)
	B2	2.20(2)		2 Ir1	2.13(3)
	B3	2.32(2)		Ir2	2.32(2)
	2 B3	2.36(2)		2 Ir2	2.36(2)
	Ir1	2.8540(9)			
	2 Ir2	2.8842(3)			
	2 Ir1	3.0156(8)			
	2 Ir1	3.0876(9)			

[a]For bonds involving B3 a random (disordered) occupation rendering the formation of boron chain fragments is considered.

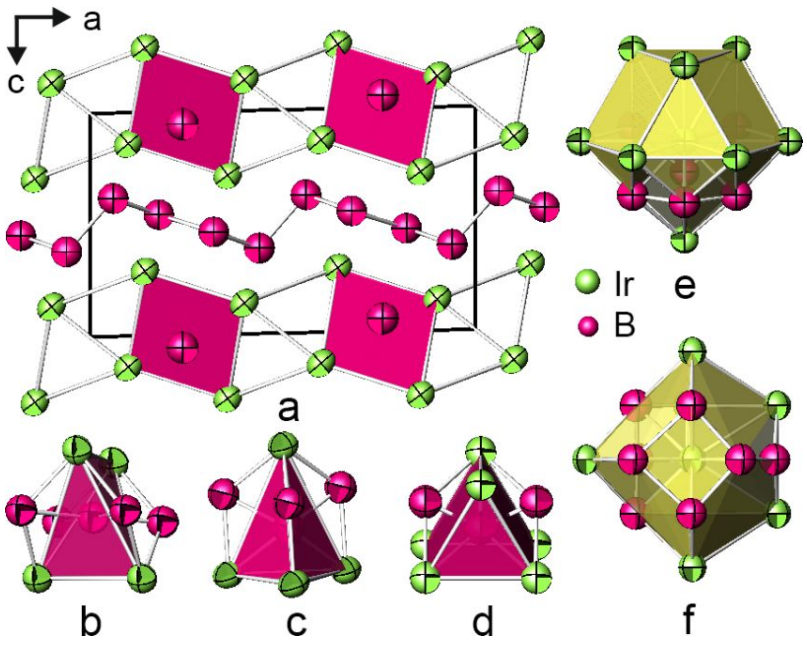

Figure 2. Crystal structure of α-Ir_2B_{3-x} as arrangement of puckered iridium layers with boron in trigonal-prismatic [Ir_6] interstices, interleaved with puckered boron layers (a). Coordination polyhedra of atoms B1 (b), B2 (c), B3(d), Ir1 (e) and Ir2 (f). The figures reflect the presence of boron in every [Ir_6] trigonal prism.

3.2. Crystal structure of β-Ir_2B_{3-x}

The existence of an unknown boron-rich iridium phase was initially obtained in the sample of approximate composition ~$Ir_{50}B_{50}$ (in at. %) via high temperature synthesis in the radio frequency induction furnace. The X-ray powder diffraction revealed, besides monoclinic α-Ir_2B_{3-x} and traces of tetragonal Ir_5B_4, the pattern of an unknown phase, which was indexed as an orthorhombic unit cell (*a*~10.77 Å, *b*~2.84 Å, *c*~6.04 Å). The powder X-ray diffraction pattern of the $Ir_{44}B_{56}$ (in at.%) alloy, arc-melted and annealed at 900 °C, exhibited significantly larger amounts of the orthorhombic phase and only α-Ir_2B_{3-x} as impurity phase; consequently, it was used for further structural studies. Lattice parameters and intensities of reflections of this powder pattern were consistent with those recently established for the high pressure /high temperature compound with nominal composition Ir_4B_5 by Petermüller et al. (2018).[38] Rietveld refinements of powder diffractograms of α- and β-Ir_2B_{3-x} (applying structural models obtained from single crystal studies in the current work for α-Ir_2B_{3-x} and in Ref. 38 for β-Ir_2B_{3-x}) revealed good correspondences between experimental and calculated XRPD intensities and converged with reasonable values of reliability factors (Figure 3 and Footnote Table 3). For two iridium atoms in β-Ir_2B_{3-x} the positional and displacement parameters as well as occupancies were determined, unambiguously defining the metal substructure. For B1 and B2, the positional parameters were refined while the occupancies and displacement parameters for these two atoms were fixed during refinement. Owing to the very small scattering power of the light element, the boron positional parameters, occupation factors and displacement parameters in the crystal structures of metal borides that contain heavy metal atoms are difficult to determine from X-ray powder diffraction data, particularly for the B-deficient atom position. Therefore, the atom coordinates, occupancy and displacement parameter of B3 in the partially occupied atom position were not refined, but accepted from single crystal data reported in the literature.[38] The X-ray powder diffraction pattern of the sample obtained via high-temperature synthesis is given in Figure S1.

Similarly to α-Ir_2B_{3-x}, the crystal structure of β-Ir_2B_{3-x} exhibits infinite columns of Ir trigonal prisms partially filled with boron atoms and extending along the *b*-direction. Four columns of trigonal prisms interconnect in the *ac* plane via Ir-Ir bonds to form channels accommodating ribbons of two interlinked zigzag chains of boron atoms. Both Ir1 and Ir2 in β-Ir_2B_{3-x} exhibit 13-fold coordination (six Ir and seven B), in contrast to iridium atoms in α-Ir_2B_{3-x}, which have larger coordination numbers (CN=14 and CN=15 for Ir1 and Ir2, respectively) (Figure 4, Table 3). Ir2 in both structures coordinates the boron quadrilaterial units, however, the values of B-B bond lengths within these units in β-Ir_2B_{3-x} are less spread out, i.e. 1.96(2) Å for B1-B2 and 2.13(2) Å for B1-B1 in α-Ir_2B_{3-x} vs 2.05 Å for B1-B2 and 2.08 Å for B1-B1 in β-Ir_2B_{3-x}. The atomic environments around boron atoms in the two structures appear similar (i.e. tetrahedra of iridium with four tetrahedrally coordinated boron atoms against the edges for B1 ([$B1B_4Ir_4$]) and double-capped iridium trigonal prisms for B3

([$B3B_2Ir_6$])), except for atoms B2, which are located at the edge of the ribbons and are six-fold coordinated ([$B2B_2Ir_4$]).

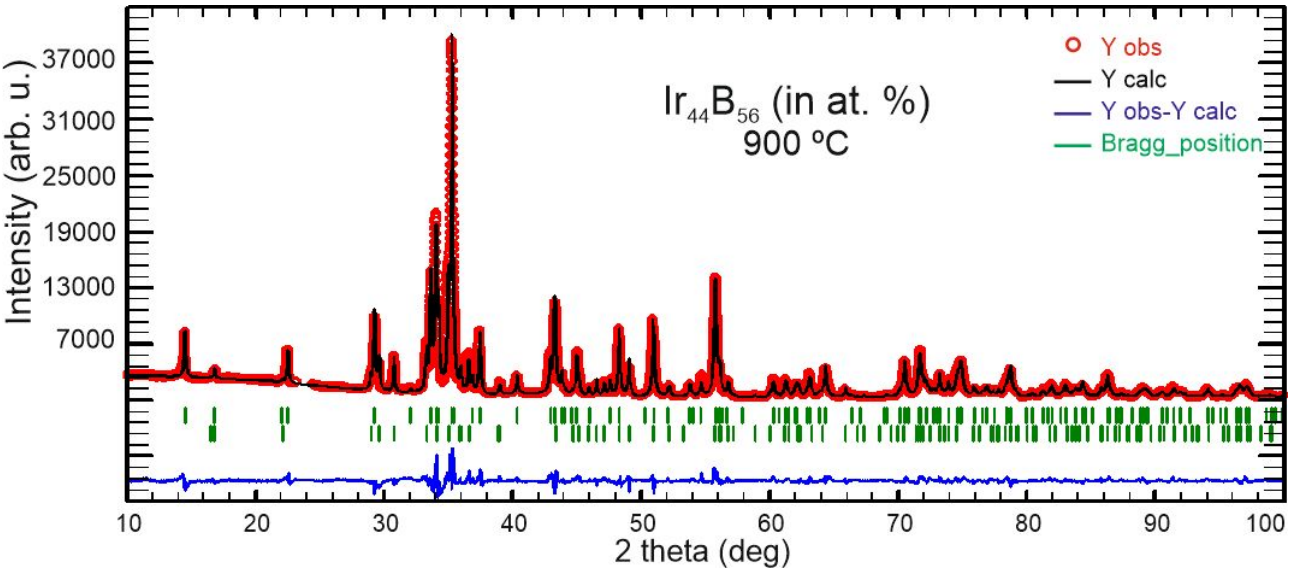

Figure 3. Rietveld X-ray powder diffraction refinement for α-Ir_2B_{3-x} (space group *C*2/*m*, R_I=0.0556, R_f=0.0276; upper row of Bragg positions) and β-Ir_2B_{3-x} (space group *Pnma*, R_I=0.0675, R_f=0.0413; lower row of Bragg positions).

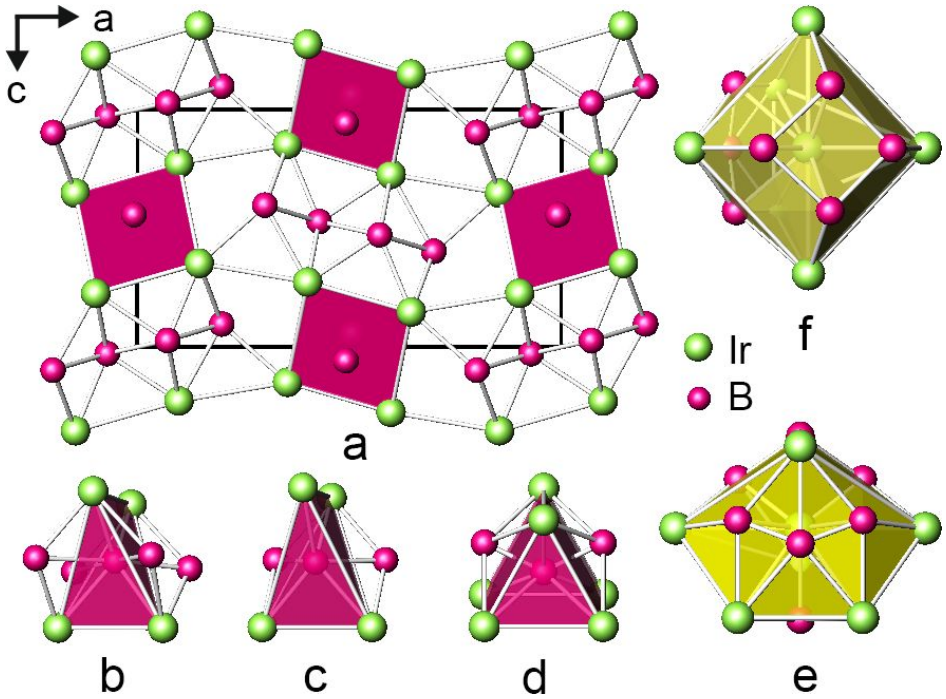

Figure 4. Crystal structure of β-Ir_2B_{3-x} as arrangement of boron filled Ir_6 trigonal prisms (red) and ribbons of condensed B-B zigzag chains (a). Coordination polyhedra of atoms B1 (b), B2 (c), B3(d), Ir1 (e) and Ir2 (f). The figures reflect the presence of boron in every [Ir_6] trigonal prism.

Table 3. Interatomic distances in β-Ir_2B_{3-x} (Å) [a,b]

Ir1 –	B3	2.07	B1 – 2	B2	2.05
	2 B3	2.13		2 Ir2	2.07
	2 B2	2.17		2 B1	2.08
	B2	2.19		Ir2	2.17
	B1	2.20		Ir1	2.20
	Ir2	2.7360			
	Ir2	2.8023	B2 –	2 B1	2.05
	2 Ir1	2.8319		2 Ir1	2.17
	2 Ir2	2.9397		Ir1	2.19
				Ir2	2.27
Ir2 – 2	B1	2.07			
	B1	2.17	B3 – 2	B3	1.58
	B3	2.20		Ir1	2.07
	2 B3	2.22		2 Ir1	2.13
	B2	2.27		Ir2	2.20
	Ir1	2.7360		2 Ir2	2.22
	Ir1	2.8023			
	2 Ir2	2.8319			
	2 Ir1	2.9397			

[a]Calculated from crystal structure data obtained from Rietveld refinement of powder pattern: space group *Pnma*; *a*=10.7519(3) Å, *b*=2.83193(7) Å, *c*=6.0293(1) Å; Ir1 in 4*c*, *x*=0.8513(4), *y*=¼, *z*=0.3574(4), Oc=1.00(1), B_{iso}=0.67(3); Ir2 in 4*c*, *x*=0.5949(4), *y*=¼, *z*=0.2737(4), Occ.=1.00(1), B_{iso}=0.54(6); B1 in 4*c*, *x*=0.57(1), *y*=¾, z=0.52(1), Occ.=1.0, B_{iso}=0.8; B2 in 4*c*, *x*=0.80(1), *y*=¾, *z*=0.10(1), Occ.=1.0, B_{iso}=0.8; B3 in 4*c*, *x*=0.0080, *y*=¼, *z*=0.5570, Occ.=0.5, B_{iso}=0.8. Isotropic displacement parameters and occupancies of B atoms were fixed during refinement. For B3, the fixed values of atom coordinates obtained from single crystal diffraction study[38] were applied. [b]For bonds involving B3, a random (disordered) occupation rendering the formation of boron chain fragments is considered.

3.3. Density function theory calculations

In the course of structure relaxation of *α*-Ir_2B_{3-x} and *β*-Ir_2B_{3-x} using the models that assume full occupations of B3 positions of both models the crystallographic parameters were optimized and are presented in Table 4 and Table 5, respectively. Both structures exhibit notable divergence (around 10%) between the experimentally obtained cell parameter *b* and the values obtained as a result of cell relaxation procedure for both full relativistic and scalar relativistic calculations. This behavior makes sense and is attributable to the discrepancy between the models applied for calculations and the actual crystal structures exhibiting partially occupied atomic positions of B3 in *α*-Ir_2B_{3-x} and *β*-Ir_2B_{3-x} thus decreasing the experimentally observed cell parameter *b*. The remaining cell parameters including the monoclinic angle *β* for *α*-Ir_2B_{3-x} as well as atomic positions, obtained as a result of cell relaxation are in good agreement with the experimental data. We should note here that neglecting the partial

occupation of B3 located in trigonal prismatic interstices (metal-boride subunit of both Ir_2B_{3-x} structural modifications) does not affect the general picture of bonding derived from our calculation and described in the next paragraph. This methodology was justified as well by good agreement between calculated and experimental characteristics which resulted from stress-strain calculations for β-Ir_2B_{3-x} (denoted as β-Ir_4B_5).[38]

Table 4. Atomic coordinates and cell parameters of α-Ir_2B_3 obtained as a result of cell relaxation procedure (space group *C2/m*, no. 12)

	α-Ir_2B_3[a]	α-Ir_2B_3[b]	α-Ir_2B_3[c]
a (Å)	10.37869	10.32722	10.5515
b (Å)	3.11661	3.13359	2.8842
c (Å)	6.08300	6.072257	6.0965
β (deg)	91.122	91.031	91.121
Ir1 in 4*i* (*x*,0,*z*)	*x*=0.10213	*x*=0.10085	*x*=0.09953
	z=0.14363	*z*=0.14567	*z*=0.13822
Ir2 in 4*i* (*x*,0,*z*)	*x*=0.35867	*x*=0.35969	*x*=0.35744
	z=0.29431	*z*=0.29322	*z*=0.28831
B1 in 4*i* (*x*,0,*z*)	*x*=0.17412	*x*=0.17452	*x*=0.17883
	z=0.47415	*z*=0.47542	*z*=0.45906
B2 in 4*i* (*x*,0,*z*)	*x*=0.55846	*x*=0.55916	*x*=0.56031
	z=0.38311	*z*=0.38376	*z*=0.38263
B3 in 4*i* (*x*,0,*z*)	*x*=0.74084	*x*=0.74025	*x*=0.74036
	z=0.08074	*z*=0.07948	*z*=0.05650

[a]calculated without SOC; [b]with SOC; [c]experimental values obtained from single crystal X-ray diffraction data refinement. Full occupancy of B3 atom position was assumed during the calculations.

Table 5. Atomic coordinates and cell parameters of β-Ir_2B_3 obtained as a result of cell relaxation procedure (space group *Pnma*, no. 62)

	β-Ir_2B_3[a]	β-Ir_2B_3[b]	β-Ir_2B_3[c]
a (Å)	10.55991	10.56308	10.7519(3)
b (Å)	3.17506	3.17455	2.83193(7)
c (Å)	5.87137	5.87151	6.0293(1)
Ir1 in 4*i* (*x*,¼,*z*)	*x*=0.85139	*x*=0.85130	*x*=0.8513(4)
	z=0.35815	*z*=0.35810	*z*=0.3574(4)
Ir2 in 4*i* (*x*,¼,*z*)	*x*=0.59896	*x*=0.59902	*x*=0.5949(4)
	z=0.27890	*z*=0.27882	*z*=0.2737(4)
B1 in 4*i* (*x*,¾,*z*)	*x*=0.57508	*x*=0.57511	*x*=0.57(1)
	z=0.51633	*z*=0.51636	*z*=0.52(1)
B2 in 4*i* (*x*, ¾,*z*)	*x*=0.80272	*x*=0.80282	*x*=0.80(1)1
	z=0.10687	*z*=0.10684	*z*=0.10(1)
B3 in 4*i* (*x*,¼,*z*)	*x*=0.01272	*x*=0.01262	*x*=0.008
	z=0.58550	*z*=0.58552	*z*=0.557

[a]calculated without SOC; [b]with SOC; [c]experimental values obtained from Rietveld refinement of X-ray powder diffraction data, see Footnote Table 3.

Late transition element based materials, particularly those including iridium, evoke growing interest in the materials physics due to several factors, i.e. they tend to exhibit wide electronic bands with relatively weak electronic correlations and strong crystal field effects as well as they are inclined to show strong spin-orbit coupling effects due to the large atomic mass associated with 5d elements.[60] However, in our study we observed that the spin-orbit coupling for α-Ir_2B_{3-x} and β-Ir_2B_{3-x} has a very modest effect on the electronic density of states around the Fermi level, making the results of calculations without and with SOC almost undistinguishable (Figure 5).

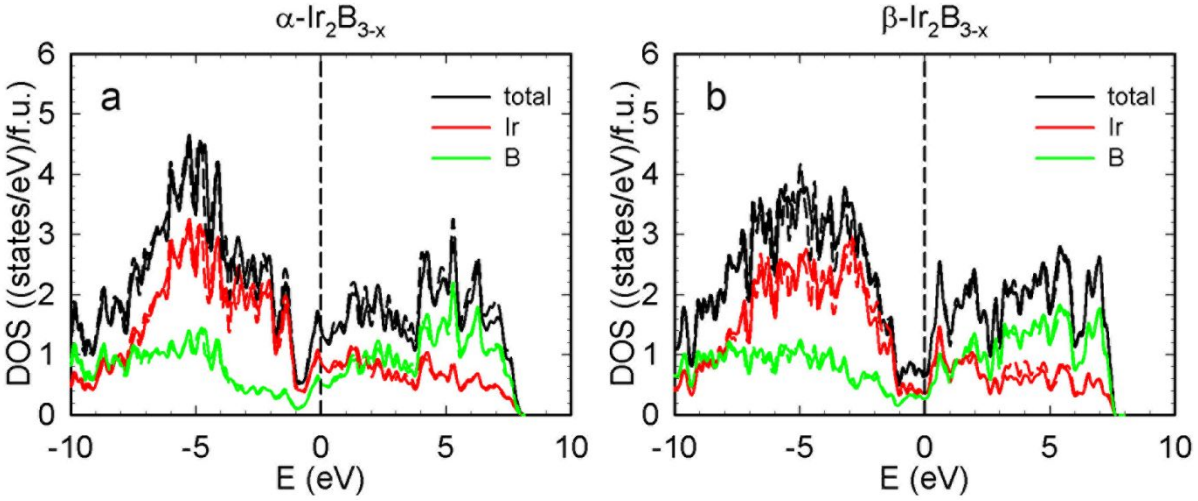

Figure 5. Electronic density of states of α-Ir_2B_{3-x} (a) and β-Ir_2B_{3-x} (b). Solid and dashed lines correspond to the values calculated without and with SOC respectively.

Densities of states below the Fermi level of α-Ir_2B_{3-x} and β-Ir_2B_{3-x} are governed by states of iridium atoms. In case of α-Ir_2B_{3-x} the electron density of states at the Fermi level is equal to 1.41 states/eV*f.u. It consists of the dominant states of Ir with the averaged electron density value of 0.44 states/eV*atom and states of boron with significantly lower averaged electron density of 0.18 states/eV*atom. Calculations of the electron density of states of β-Ir_2B_{3-x} show the existence of pseudo gap in the range between -1 and 0 eV. At the Fermi level the eDOS of β-Ir_2B_{3-x} is characterized by a value of 0.64 states/eV*f.u. In the case of this structural modification of the compound the cumulative influences of boron and iridium electron states on the Fermi level are equal. Above the Fermi level the density of states of both compounds is governed by the states of boron.

Partial electron densities of states are presented in Figure S2 and Figure S3 for α-Ir_2B_{3-x} and β-Ir_2B_{3-x} respectively. As can be seen from the graphs, the effects of spin orbit coupling on the

electron density of states are negligible. For both structural modifications, the electron densities of states are dominated by the sum of Ir *d*- and B *p*- states both above and below the Fermi level.

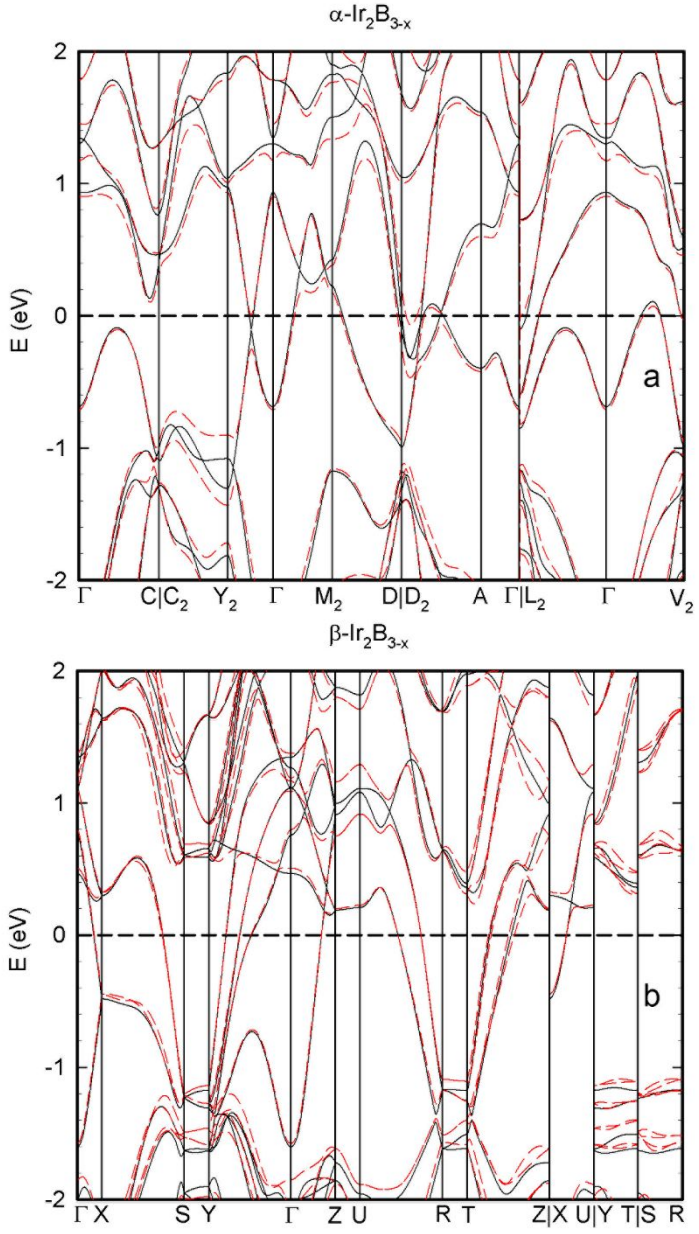

Figure 6. Electronic band structure of α-Ir_2B_{3-x} (a) and β-Ir_2B_{3-x} (b). Solid and dashed lines correspond to the values calculated without and with SOC respectively.

Electronic band structures of α-Ir_2B_{3-x} and β-Ir_2B_{3-x} are presented in Figure 6 for a non-spin-orbit case (solid lines) and with involvement of spin-orbit interactions (dashed lines). The compounds are expected to be metallic due to a number of bands crossing the Fermi level in both calculations with and without SOC. Electronic band structure of α-Ir_2B_{3-x} is characterized by a Dirac like anomaly between Y_2 and Gamma where the spin-orbit coupling provokes the anticrossing of the electron bands

near the Fermi level. The other feature characterizing the band structure of α-Ir_2B_{3-x} is the spin-orbit coupling induced inversion of bands at around 0.2 eV in Gamma-M_2 region. The influence of spin-orbit coupling on the electronic band structure of *β*-Ir_2B_{3-x} is much less pronounced.

3.4. Bonding in *α*-Ir_2B_{3-x} and *β*-Ir_2B_{3-x}

The crystal structure of *α*-Ir_2B_{3-x} can be viewed as an arrangement of a metal boride partial structure (two corrugated layers of iridium extending along *b* with boron atoms in interstices in trigonal prismatic coordination [$B3Ir_6$]), separated by a boron layer composed of ribbons of corrugated B_6 hexagons, interlinked via B-B external bonds. A calculation of the electron localization function (Figure 7) shows relatively high levels of electron localization for B3-Ir bonds within the trigonal prismatic part of structure with a maximal value of 0.704 for B3-Ir1 bonds (distance B3-Ir1 2.13(3) Å) and slightly reduced ELF of 0.652 for B3-Ir1 and 0.615 for B3-Ir2 suggesting a moderate covalent contribution of the latest two bonds in the Ir-B interaction within [$B3Ir_6$] trigonal prisms (Figure 7b). In case of the formation of boron chain fragments in Ir trigonal prisms, the ELF distribution between B3 is characterized by an ELF_{max} value of 0.706, indicating covalent bonding (Figure 7a).

B1 and B2 form boride layers, where B1-B2 and B2-B2 bonds participate in formation of puckered hexagons which are inter-connected via B1-B1 bonds (Figure 7f). A high ELF of ~0.750 between B2 atoms and slightly smaller electron localization function domains between B1-B2 (ELF: ~0.675) prove strong covalent bonding in the corrugated hexagonal rings (Figure 7d, Figure S4a). Rather small values of ELF (max ~0.54) appear for B1-B1 bonds (Figure 7e), revealing a small probability of electrons pairing in the boron quadrilaterial units, formed between ribbons of covalently bonded boron hexagons. The apparently minor covalent bonding character of B1-B1 interaction could be expected from the rather large distance of 2.13(2) Å between these two atoms, as compared to other B-B bonds in the structure. B2 is tetrahedrally bonded with iridium atoms from adjacent metal-boride layers (Figure 2). Strong covalent bonding is obvious from the ELF distribution maps for both B1-Ir1 and B1-Ir2 interactions (ELF>0.710) (Figure 7c, Figure S4b). The maxima of ELF for B2-Ir2 contacts are 0.697 for a longer contact and 0.749 for a shorter contact (Table 2); the calculated ELF map revealed a maximum of 0.738 for the B2-Ir1 bond, which is significantly shifted to boron along the line indicating geometrical bond (Figure 7g).

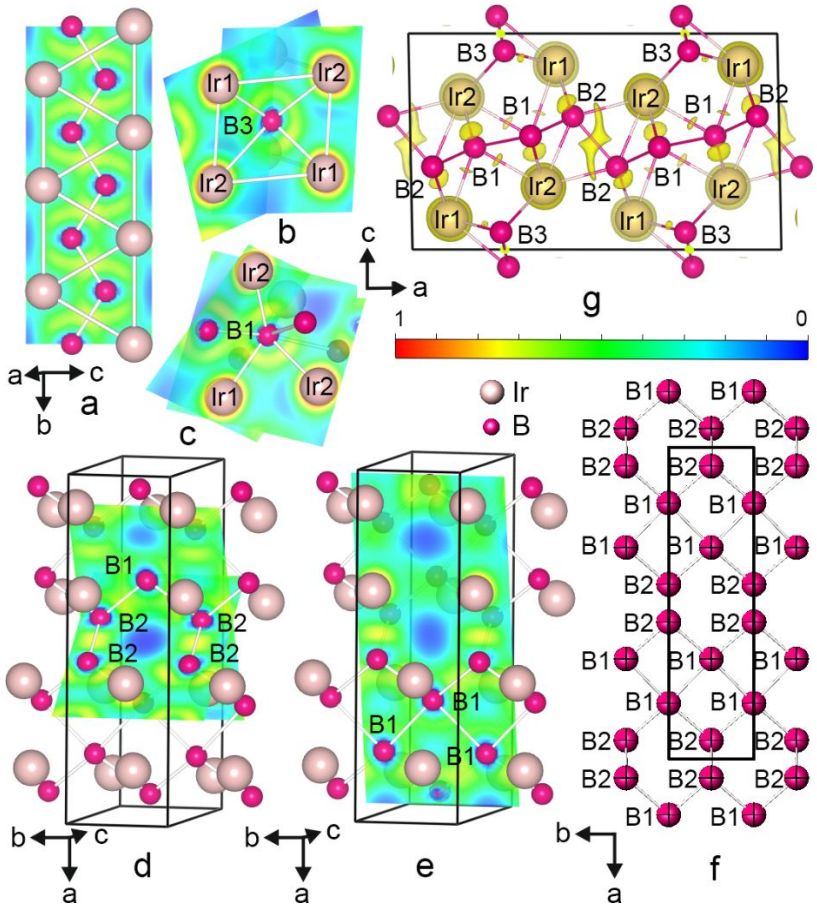

Figure 7. Sections of calculated electron localization function in α-Ir_2B_{3-x} structure within the planes visualizing: B3-B3 bonding on the assumption of formation of boron chain fragments (a); boron – iridium covalent bonding in trigonal prisms (b); B1-Ir1 and B1-Ir2 interactions (c); boron interactions in puckered boron hexagons (d) and B squares (e); boron layer as obtained from single crystal X-ray data refinement (f). Electron localization at 0.70 isosurface level (g). Constructed ELF sections assume full occupancy for the B3 atom position.

In comparison to α-Ir_2B_{3-x}, the β-Ir_2B_{3-x} structure exhibits a combination of the infinite columns of iridium trigonal prisms half filled with boron and the ribbons of double boron chains. The calculated ELF for β-Ir_2B_{3-x} are shown in Figure 8 and Figure S5, which clearly reveals the presence of strong covalent bonds between boron and iridium atoms with the maximum value of 0.785 for B1-Ir2 (B1-2Ir2 2.07 Å) (Figure 8a). The ELF values for B1-Ir2 and B1-Ir1 bonds, which complete the tetrahedral coordination of B1 are 0.739 and 0.712, respectively, both within the covalent region (Figure 8a). Similarly, high values of ELF have been found between iridium atoms and B2, which is located at the edge of the boron ribbon, i.e. three bonds B2-Ir1 (at 2.17 Å and 2.19 Å) have ELF value 0.777, while the longer contact B2-Ir2 (2.27 Å) has a lower value ELF: 0.695 (Figure 8b). The high value of electron localization function is also identified in the trigonal prisms between B3 and iridium

atoms (ELF: 0.689 and 0.630 for B3-Ir1 and B3-Ir2 contacts, respectively) (Figure 8c). Assuming the formation of B3-B3 chain fragments in iridium trigonal prisms, the bond between boron atoms has the ELF value 0.648 (Figure 8d). In contrast, the ELF maps within the planes in the boron ribbons reveal large green zones, indicating a small probability of electron pairing (ELF: 0.625 for B1-B2 bond) with particularly small values of ELF (i.e. 0.525) in the region between boron chains (B1-B1 contact) (Figure 8e-f). Calculated Bader charges show substantial charge transfer from boron atoms to the atoms of iridium for both compounds studied (Table 6).

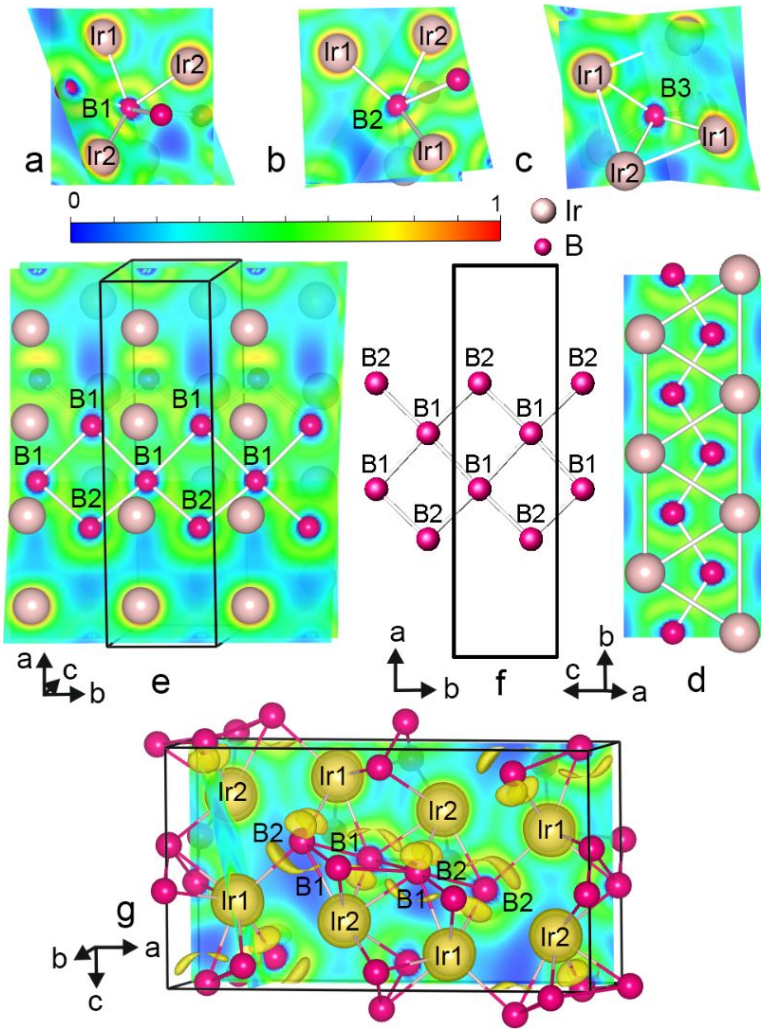

Figure 8. Sections of calculated electron localization function in β-Ir_2B_{3-x} structure within the planes visualizing: covalent Ir-B bonding in [BIr_4] tetrahedra (a, b) and [BIr_6] trigonal prism (c); B3-B3 bonding on the assumption of formation of boron chain fragments (d); B1-B1 and B1-B2 interaction (e). Boron substructure consisting of branched zigzag chains formed by B1 and B2 (e). Electron localization at 0.69 isosurface level complemented with the planes sections showing Ir1-Ir2 interaction within the 8-membered Ir cage (g). Constructed ELF sections assume full occupancy for the B3 atom position.

Table 6. Calculated Bader charges of Ir and B atoms in α- and β-Ir_2B_{3-x} phases

Phase	Space group	Atom	Charge value (e^-)
α-Ir_2B_{3-x}	*C*2/*m*	Ir1 Ir2 B1 B2 B3	-0.52 -0.50 +0.48 +0.34 +0.20
β-Ir_2B_{3-x}	*Pnma*	Ir1 Ir2 B1 B2 B3	-0.57 -0.48 +0.50 +0.31 +0.23

4. DISCUSSION

Among layered boride structures, there are only few representatives exhibiting a chair-like configuration of hexagons consistent with the structure of diamond. Examples are c-BN with ordered boron and nitrogen atoms forming hexagonal chair-like rings;[61] ReB_2[11] (and a number of solid solutions with this structure type[8]) where layers of condensed hexagons in chair-like conformation interleave with planar layers of metal atoms, Ru_2B_3 which is composed of layers of condensed chair-like puckered hexagons, alternated with two planar layers of metal atoms orderly filled with boron in interstices (WC-type block); [62] Mo_2B_4 and W_2B_4, showing stacking sequences of two types of boron atom layers (chair-like corrugated layers and graphite-like planar layers) interleaved with metal atom layers[63] or two recently synthesized high-pressure borides with ReB_2-type related structures, ReB_3 and ReB_4.[64] Some of these structures, together with α-Ir_2B_{3-x}, are shown in Figure S6. These structures are intensively explored both experimentally and theoretically as potential candidates for hard and incompressible materials due to strong covalent bonding within the boron substructure.[40,65-70]

Despite different condensation of boron units within boron sheets, the conformation of boron hexagons in α-Ir_2B_{3-x} corresponds to that in ReB_2. Moreover, similarly to Ru_2B_3, α-Ir_2B_{3-x} exhibits double metal layers. Owing to these features, the structure fits in a series of layered ReB_2-type related structures. Further discussion aims to elucidate the differences in bonding in boron substructures and metal-boron bonds at the interlayers between two modifications in comparison with bonding in ReB_2 as related structure.

The hexagonal units in boron puckered sheets reveal considerably different lengths of B-B contacts, i.e. 1.93 Å and 1.96 Å in α-Ir_2B_{3-x} while all B-B contacts in ReB_2 are equal, i.e. 1.822 Å.[11] The central shortest B2-B2 bonds (~1.93 Å, Figure 7f) in corrugated B_6 units in α-Ir_2B_{3-x} have the largest ELF values, reminiscent to that in ReB_2, [67,69] while the longer contacts have significantly smaller ELF, compared to ReB_2. The ELF maxima observed between B2-B2 in α-Ir_2B_{3-x} seem to be

smeared and displaced along the B2-Ir2 contact in analogy to ELF in ReB_2. The major difference between ReB_2 and α-Ir_2B_{3-x} boron substructures consists in condensation of hexagonal rings via external elongated B1-B1 bond (~2.13 Å) in the latter compound, where the value of calculated ELF indicates the electron-gas-like pair probability. A comparative analysis of M-B bonds at the interlayers shows that the metal atom in ReB_2-type structure is situated above the B atom; B atoms are coordinated by four Re, forming triangular-based pyramids Re_4, exhibiting almost equal B-Re distances within 2.23 Å - 2.26 Å. In α-Ir_2B_{3-x}, the atom coordination of B2 corresponds to that of boron in ReB_2, notwithstanding different values of B2-Ir distances (2.12 Å – 2.20 Å). Similarly to ReB_2, ELF for B2-Ir bonds are not equal being the smallest for the B2-Ir2 contacts within the (010) plane (Figure S4). B1 in α-Ir_2B_{3-x} (i.e. terminating atoms in B hexagonal ribbons) is located in a Ir_4 tetrahedron, in which two Ir2 atoms are strongly covalently bonded with central B1 atom (at 2.15 Å).

Boron ribbons in β-Ir_2B_{3-x} are composed of boron zigzag chains bounded via external bonds to form quadrilaterial boron units. Here the two kinds of boron atoms are tetrahedrally surrounded by four Ir atoms each. The Ir-B bonds are characterized by rather spread out values of ELF (Figure S5). In [$B1Ir_4$] tetrahedra, three B1-Ir bonds are of comparable strength while the remaining one is much weaker. Similarly, B2 generates three strong covalent bonds and one weaker covalent bond with iridium atoms; the ELF values of B2-Ir bonds are more uniform as compared to B1-Ir bonds. In contrast to α-Ir_2B_{3-x}, only very modest values of electron localization function were observed between boron atoms in the boron substructure of β-Ir_2B_{3-x} (Figure 7 and Figure 8, respectively).

Remarkably, as was already mentioned above, the hardness of β-Ir_2B_{3-x} (denoted as β-Ir_4B_5) [38] was reported to be noticeably lower than the hardness of the α-Ir_2B_{3-x} modification. Comparing the bonding features elucidated in the current work, we conclude that the dissimilar values of hardness for the two modifications could be a consequence of extremely reduced covalent bonding within a slightly corrugated quadrilaterial boron subunits in β-Ir_2B_{3-x} as compared to strong covalent interaction in the layers of interlinked boron hexagons in a-Ir_2B_{3-x}.

The coordination polyhedron of B3 is an Ir_6 trigonal prism in both a- and β-Ir_2B_{3-x},; trigonal prisms condense in columns via common rectangular faces. In a-Ir_2B_{3-x}, the columns of Ir_6 trigonal prisms connect together in puckered layers via Ir-Ir bonds creating empty octahedra and tetrahedra (Figure 9a); in β-Ir_2B_{3-x} the face-shared columns of Ir_6 trigonal prisms interconnect to form empty rectangular pyramids and tetrahedra (Figure 9b). The trigonal prismatic metal environment of boron can be found in many boride families, including CrB and AlB_2. The M/B ratio in both compounds is within the concentration range of formation of binary borides (e.g. CrB, V_2B_3, Ta_3B_4) which constitute the boride partial structure of MAB phases and exhibit some common futures such as metal layers, trigonal prismatic environment of B atom and formation of fragments of boron zigzag chains in metal boride substructure. At variance to ReB_2 (Figure 9e) or Ru_2B_3 (Figure 9f) structures, in which

the boron atoms of the chair-like hexagons are located in the triangular M_4 pyramids (Figure 9g), the B atoms in the *a*-Ir_2B_{3-x} are placed in Ir_4 tetrahedra and Ir_4 triangular pyramids (Figure 9h). In *β*-Ir_2B_{3-x}, the B1 and B2 occupy tetrahedral Ir_4 vacancies (Figure 9i).

The analysis of structural similarities of *a*- and *β*-Ir_2B_{3-x} with the structures of MAB phases, e.g. Cr_2AlB_2 (Mn_2AlB_2-type, *Cmmm* space group; a layer of Al is located between Cr/B partial structure, Figure 9j) and ReB_2-type related structures indicate that other borides based on similar structural principles may exist and calls for further experiments to verify this suggestion.

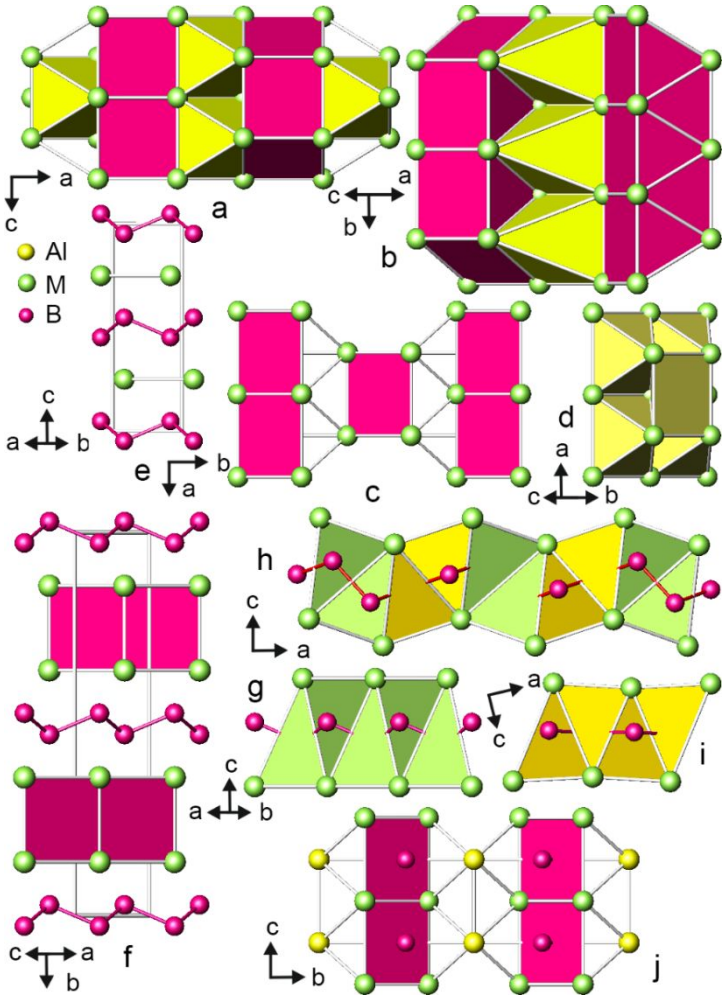

Figure 9. Columns of trigonal prisms (red), empty octahedra (gold) and empty tetrahedra (left open) in *a*-Ir_2B_{3-x} (a). Columns of trigonal prisms (red), empty rectangular pyramids (gold) and empty tetrahedra (left open) in *β* -Ir_2B_{3-x} (b). Crystal structure of CrB as arrangement of trigonal prisms [BCr_6] (c). Empty rectangular pyramids (gold) and tetrahedra (left open) in CrB structure (d). Crystal structure of ReB_2 (origin shift ½,½,0) (e). Crystal structure of Ru_2B_3 (f). [BRe_4] triangular pyramids in ReB_2 (g). [$B1Ir_4$] tetrahedra (gold) and [$B2Ir_4$] triangular pyramids (green) in *a*-Ir_2B_{3-x} (h). [BIr_4] tetrahedra in *β*-Ir_2B_{3-x} (i). Crystal structure of Cr_2AlB_2 as arrangement of trigonal prisms [BCr_6] (j).

CONCLUSIONS

Two structural modifications of binary iridium boride, α-Ir_2B_{3-x} and β-Ir_2B_{3-x} (formerly obtained at high pressure and high temperature) have been synthesized at ambient conditions via both arc-melting and high temperature synthesis. The crystal structure of layered α-Ir_2B_{3-x} was studied from single crystal and powder X-ray diffraction (space group *C*2/*m*). Refinement of single crystal data clearly showed ordered distribution of Ir atoms and the vacancies on one B site, resulting in the formula Ir_2B_{3-x}, (x=0.54). Structural parameters of β-Ir_2B_{3-x} were obtained from powder X-ray diffraction data (space group *Pnma*).

α-Ir_2B_{3-x} is built of ribbons of boron chair-like hexagons (ReB_2-type boron unit), interlinked via external bonds in layers and interleaved along the *c*-direction with two corrugated layers of iridium. An additional boron (Occ. 0.46(7)) is found in interstices of puckered iridium bi-layers in [BIr_6] trigonal prismatic coordination. The boron substructure in β-Ir_2B_{3-x} comprises ribbons built up of slightly corrugated quadrilaterial boron units running along *b*-direction and located in 8-membered iridium cages. The α-Ir_2B_{3-x} phase reveals common structural features with ReB_2-type and related structures (Ru_2B_3, Mo_2B_4, W_2B_4, etc). On the other hand, α-Ir_2B_{3-x} demonstrates as well some commonalities with CrB-, V_2B_3-, Ta_3B_4-structures, such as layered arrangement of metal atoms, condensed boron filled Ir_6 trigonal prisms, potential formation of fragments of boron zigzag chains in the metal boride substructure. However, besides the difference of trigonal prisms condensation in layers, i.e. face- and base-shared in e.g. CrB structure and interconnected via Ir-Ir bonds in α-Ir_2B_{3-x}, significant distinctions occur at the stacking of layers of interlinked trigonal prisms. In the CrB structure the adjacent layers are connected via empty rectangular-based pyramids Cr_5 and empty tetrahedra Cr_4, while in α-Ir_2B_{3-x} the voids between the puckered layers are occupied by boron atoms in tetrahedral Ir_4 and triangular-based pyramidal Ir_4 coordination.

Both α-Ir_2B_{3-x} and β-Ir_2B_{3-x} are expected to be metallic from the DFT calculations with several bands crossing the Fermi level in both calculations with and without SOC. The β-Ir_2B_{3-x} is characterized by a pseudogap around the Fermi level and a small eDOS of 0.6405 states/eV*f.u. at $E=E_F$. The eDOS of α-Ir_2B_{3-x} is 1.405 states/eV*f.u.

Bonding in α- and β-Ir_2B_{3-x} was investigated using the electron localization function. Large values of ELF indicate covalent bonding interaction between B atoms in the core part of boron hexagons in boron layers of α-Ir_2B_{3-x}. In contrast, the B-B bonds in the B_4 units have relatively small ELF values, corresponding to metallic bonds. ELF values between Ir and B atoms imply mixed covalent and metallic bonding between iridium and boron layers. From this, in the context of the density of states analysis described above, we conclude that covalent B-B bonds within boron hexagons and covalent Ir-B bonds are the factors affecting hardness of monoclinic and orthorhombic Ir_2B_{3-x} phases. Obtained results suggest that enhancing the strength of the chemical bonds between

layers is significant to design new harder transition metal borides with layered structure. Our conclusions agree well with results reported for the related transition metal boride systems.

ASSOCIATED CONTENT

Supporting Information

The Supporting Information is available free of charge at ....

The Supporting Information includes: Powder X-ray diffraction pattern of ~$Ir_{50}B_{50}$ (in at. %) sample obtained from high-temperature synthesis and crystallographic characteristics of the phases elucidated from Rietveld refinement; Partial electron densities of states of individual atoms in α-Ir_2B_{3-x} and β-Ir_2B_{3-x} structures calculated with and without SOC; Sections of calculated electron localization function in α-Ir_2B_{3-x} and β-Ir_2B_{3-x} visualizing boron-iridium bonding; Unit cells of a series of boride structures exhibiting chair-like configuration of boron hexagons in comparison with α-Ir_2B_{3-x}.

Accession Codes

CSD 2371295 (α-Ir_2B_{3-x}) contain the supplementary crystallographic data for this paper. These data can be obtained free of charge via....

AUTHOR INFORMATION

Corresponding Author

Oksana Sologub - *Institute of Solid State Physics, TU Wien, A-1040 Vienna, Austria;* orcid.org/0000-0003-2168-1901; E-mail: oksana.sologub@univie.ac.at

Authors

Leonid P. Salamakha - *Institute of Solid State Physics, TU Wien, A-1040 Vienna, Austria; Department of Physics of Metals, L'viv National University, L'viv, Ukraine;* orcid.org/0000-0002-7997-9463

Berthold Stöger - *X-Ray Center, TU Wien, A-1060 Vienna, Austria;* orcid.org/0000-0002-0087-474X

Takao Mori - *National Institute for Materials Science (NIMS), Research Center for Materials Nanoarchitectonics (MANA), Tsukuba, Japan;* orcid.org/0000-0003-2682-1846

Neven Barisic - *Institute of Solid State Physics, TU Wien, A-1040 Vienna, Austria; Department of Physics, Faculty of Science, University of Zagreb, Croatia;* orcid.org/0000-0003-4637-0544

Peter F. Rogl - *Institute of Materials Chemistry, University of Vienna, A-1090 Vienna, Austria;* orcid.org/0000-0002-7733-1612

Herwig Michor - *Institute of Solid State Physics, TU Wien, A-1040 Vienna, Austria;* orcid.org/0000-0003-1642-5946

Ernst Bauer - *Institute of Solid State Physics, TU Wien, A-1040 Vienna, Austria;* orcid.org/0000-0001-7376-5897

Complete contact information is available at:

Author Contributions

The manuscript was written through contributions of all authors. All authors have given approval to the final version of the manuscript.

Notes

The authors declare no competing financial interest.

ACKNOWLEDGEMENT

Research supported by Austrian National Science Foundation FWF P31979-N36. The support of the project FWF Project P 35945-N is highly appreciated. N.B. acknowledges the support of the Croatian Science Foundation under Project No. IP-2022-10-3382. T.M. thanks JST Mirai JPMJMI19A1 for support.

REFERENCES

1. G. Akopov, M. T. Yeung and R. B. Kaner, *Adv. Mater.*, 2017, **29**, 1604506 and the references therein.

2. M. T. Yeung, R. Mohammadi and R. B. Kaner, *Annu. Rev. Mater. Res.*, 2016, **46(1)**, 465–485.

3. B. Albert, K. Hofmann, Metal borides: versatile structures and properties. In: Handbook of Solid State Chemistry (2017) 435–453.

4. J. P. Scheifers, Y. Zhang and B. P.T. Fokwa, *Acc. Chem. Res.*, 2017, **50(9)**, 2317–2325.

5. G. Akopov, L. E. Pangilinan, R. Mohammadi and R. B. Kaner, *Apl. Materials*, 2018, **6**, 070901.

6. V. I. Matkovich, Boron and refractory borides, Springer, Berlin, 1977.

7. T. Mori, Higher borides, K.A. Gschneidner Jr., J.-C. Bunzli, V. Pecharsky (Eds.), Handbook on the Physics and Chemistry of Rare-Earths, vol. 38, North-Holland, Amsterdam (2008), pp. 105-173.

8. P. Rogl, Existence and Crystal Chemistry of Borides, in Inorganic Reactions and Methods; Zuckerman, J.J., Ed.; VCH-Publications Inc. 1991, 13(6), 84-167 and references therein.

9. J. R. Etourneau, Borides with three-dimensional boron networks, in Inorganic Reactions and Methods; Zuckerman, J.J., Ed.; VCH-Publications Inc. 1991, 13(6), 167-196 and references therein.

10. S. J. La Placa and B. Post, *Acta Crystallogr.*, 1962, **15**, 97-99.

11. M. Frotscher, M. Hölzel and B. Albert, *Z. Anorg. Allg. Chem.*, 2010, **636**, 1783–1786.

12. B. Aronsson, *Acta Chem. Scand.*, 1963, **17**, 2036−2050.

13. H. Y. Chung, M. B. Weinberger, J. B. Levine, A. Kavner, J. M. Yang, S. H. Tolbert and R. B. Kaner, *Science*, 2007, **316**, 436-439.

14. R. W. Cumberland, M. B. Weinberger, J. J. Gilman, S. M. Clark, S. H. Tolbert and R. B. Kaner, *J. Am. Chem. Soc*., 2005, **127**, 7264-7265.

15. J. P. Robinson, G. Liu, S. Ciborowski, C. Martinez-Martinez, J. R. Chamorro, X. Zhang, T. M. McQueen, K. H. Bowen and A. N. Alexandrova, *Chem. Mater*., 2017, **29**, 9892−9896.

16. Z. - W. Ji, C. - H. Hu, D. - H. Wang, Y. Zhong, J. Yang, W. - Q. Zhang and H. - Y. Zhou, *Acta Mater*., 2012, **60**, 4208-4217.

17. W. J. Zhao and J. X. Wang, *J Solid State Chem*., 2009, **182**, 1280−1286.

18. D. Y. Wang, B. Wang and X. Y. Wang, *J. Phys. Chem. C*, 2012, **116**, 21961−21966.

19. R. Kiessling, *Acta Chem. Scand.*, 1949, **6,** 603-615.

20. Y. Yu, L. E. Tergenius, T. Lundström and S. Okada, *J. Alloys Compd.*, 1995, **221**, 86-90.

21. H. Bolmgren, T. Lundström, L. E. Tergenius, S. Okada and I. Higashi, *J. Less-Common Met.*, 1990, **161**, 341-345.

22. M. Ade, H. Hillebrecht, *Inorg. Chem.,* 2015, **54 (13)** 6122–6135.

23. S. Kota, E. Zapata-Solvas, A. Ly, J. Lu, O. Elkassabany, A. Huon, W. E. Lee, L. Hultman, S. J. May, M. W. Barsoum, *Sci. Rep.,* 2016, **6,** 26475.

24. Wang, J., Ye, TN., Gong, Y. et al., *Nat. Commun.,*2019, **10,** 2284.

25. Z.P. Malik, O. Sologub, A. Grytsiv, G. Giester, P.F. Rogl, *Inorg. Chem.,* 2011, **50,** 7669–7675.

26. F. Failamani, R. Podloucky, J. Bursik, G. Rogl, H. Michor, H. Müller, E. Bauer, G. Giester, P. Rogl, *Dalton Trans.,* 2018, **47,** 3303-3320.

27. A. A. Rezaie, Z. Yan, J. P. Scheifers, J. Zhang, J. Guo, B. P. Fokwa, *J. Mater. Chem. A,* 2020, **8,** 1646-1651.

28. A. A. Rezaie, E. Lee, J. A. Yapo, B. P. T. Fokwa, *Adv. Energy Sustainability Res.,* 2021, **2,** 2100052.

29. A. Rosenkranz, D. Zambrano, A. Przyborowski, R. Shah, A.M. Jastrzębska, *Adv. Mater. Interfaces,* 2022, **9,** 2200869 (1-12) and the references therein.

30. V.G. Nair, M. Birowska, D. Bury, M. Jakubczak, A. Rosenkranz, A.M. Jastrzębska, *Adv. Mater.,* 2022, **34,** 2108840 (1-13) and the references therein.

31. C. S. Rout, P. V. Shinde, A. Patra, and S. M. Jeong, *Adv. Sci.,* 2024, **11,** 2308178.

32. Y. Zhou, H. Xiang, F. Z. Dai, Z. Feng, *J. Am. Ceram. Soc.,* 2018, **101,** 2459.

33. Y. Zhou, H. Xiang, F.-Z. Dai, Z. Feng, *J. Mater. Sci. Technol.,* 2018, **34,** 1441.

34. M. Dahlqvist, Q. Tao, J. Zhou, J. Palisaitis, P. O. Persson, *J. Rosen, J. Am. Chem. Soc.,* 2020, **142,** 18583.

35. T. Lundstrom and L. - E. Tergenius, *Acta Chem. Scand*., 1973, **27**, 3705−3711.

36. 20. I. Zeiringer, X. Cheng, X.-Q. Chen, E. Bauer, G. Giester and P. F. Rogl, *Sci. China. Mater*., 2015, **58**, 649−668.

37. Z. Xie, R. G. Blair, N. Orlovskaya, D. A. Cullen, S. H. Lapidus, D. Kata, P. Rutkowski and J. Lis, *J. Solid State Chem*., 2016, **233**, 108-119.

38. B. Petermüller, C. Neun, K. Wurst, L. Bayarjargal, D. Zimmer, W. Morgenroth, M. Avalos-Borja, I. G. Becerril-Juarez, M. J. Mühlbauer, B. Winkler and H. Huppertz, *Inorg. Chem*., 2018, **57**, 10341−10351.

39. V. Rau and A. Latini, *Chem. Mat., 2009,* **21(8)**, 1407-1409.

40. Y. Wang, L. Wu, Y. Lin, Q. Hu, Z. Li, H. Liu, Y. Zhang, H. Gou, Y. Yao and J. Zhang, *Phys. Rev. B: Condens. Matter Mater. Phys*., 2015, **92**, 174106.

41. J. Yu, M. Khazaei, N. Umezawa, and J. Wang, *J. Mater. Chem. C,* 2018, 6, 5803-5811.

42. W.-L. Li, C. Romanescu, T.R. Galeev, Z. A. Piazza, A. I. Boldyrev, L.-S. Wang, *J. Am. Chem. Soc.,* 2012, **134,** 1, 165−168.

43. D. A. Bannykh, V. V. Lozanov, T. A. Gavrilova, A. I. Beskrovny, N. I. Baklanova, *Materials,* 2022, **15(21),** 7522.

44. J. Rodriguez-Carvajal, *Physica B,* 1993, **192**, 55-69.

45. STOE and Cie GmbH X-Area 1.31.175.0, LANA 2.6.2.0, Darmstadt, Germany, 2021

46. L.J. Farrugia, WinGX and ORTEP for Windows: an update, *J. Appl. Crystallogr*., 2012, **45**, 849-854.

47. P. McArdle, ABSEN- a PC computer program for listing systematic absences and space-group determination, *J. Appl. Cryst*., 1996, **29**, 306.

48. G.M. Sheldrick, SHELXS-97, Program for the Solution of Crystal Structures. University of Göttingen. Germany. 1997.

49. G.M. Sheldrick, SHELXL-97, Program for Crystal Structure Refinement; University of Göttingen, 1997.

50. Giannozzi, P.; Baroni, S.; Bonini, N.; Calandra, M.; Car, R.; Cavazzoni, C.; Ceresoli, D.; Chiarotti, G. L.; Cococcioni, M.; Dabo, I.; Dal Corso, A.; de Gironcoli, S.; Fabris, S.; Fratesi, G.; Gebauer, R.; Gerstmann, U.; Gougoussis, C.; Kokalj, A.; Lazzeri, M.; Martin-Samos, L.; Marzari, N.; Mauri, F.; Mazzarello, R.; Paolini, S.; Pasquarello, A.; Paulatto, L.; Sbraccia, C.; Scandolo, S.; Sclauzero, G.; Seitsonen, A. P.; Smogunov, A.; Umari, P.; Wentzcovitch, R. M., J. Phys.: Condens. Matter, 2009, **21**, 395502.

51. J. P. Perdew, A. Ruzsinszky, G. I. Csonka, O. A. Vydrov, G. E. Scuseria, L. A. Constantin, X. Zhou and K. Burke, *Phys. Rev. Lett.* 100 (2008) 136406; Erratum *Phys. Rev. Lett*., 2009, **102**, 039902.

52. D. Vanderbilt, *Phys. Rev. B: Condens. Matter Mater. Phys*., 1990, **41**, 7892−7895.

53. K. Laasonen, A. Pasquarello, R. Car, C. Lee and D. Vanderbilt, *Phys. Rev. B*, 1993, **47**, 10142.

54. A. Dal Corso, *Comput. Mater. Sci*., 2014, **95**, 337−350.

55. H. J. Monkhorst and J. D. Pack, *Phys. Rev. B*, 1976, **13**, 5188−5192.

56. K. Momma and F. Izumi, *J. Appl. Crystallogr*., 2008, **41**, 653−658.

57. O. Sologub, L. Salamakha, P. Rogl, B. Stöger, E. Bauer, J. Bernardi, G. Giester, M. Waas, R. Svagera, *Inorg. Chem.,* 2015, **54,** 10958-10965.

58. P. Rogl, H. Nowotny and F. Benesovsky, *Monatsh. Chem*., 1971, **102**, 678-686.

59. P. S. Salamakha, O. L. Sologub, A. P. Goncalves, M. Almeida, *J. Alloys Compd*., 2003, **360**, 131-136.

60. J. P. Clancy, N. Chen, C. Y. Kim, W. F. Chen, K. W. Plumb, B. C. Jeon, T. W. Noh and Y.-J. Kim, *Phys. Rev. B*, 2012, **86**, 195131.

61. B. Mårlid, K. Larsson and J.-O. Carlsson, *Phys. Rev. B*, 2001, **64,** 184107.

62. M. Frotscher, A. Senyshyn and B. Albert, *Z. Anorg. Allg. Chem*., 2012, **638 (12-13)**, 2078-2080.

63. M. Frotscher, W. Klein, J. Bauer, C.-M. Fang, J.-F. Halet, A. Senyshyn, C. Baehtze and B. Albert, *Z. Anorg. Allg. Chem*., 2007, **633**, 2626-2630.

64. E. Bykova, E. Johansson, M. Bykov, S. Chariton, H. Fei, S. V. Ovsyannikov, A. Aslandukova, S. Gabel, H. Holz, B. Merle, B. Alling, I.A. Abrikosov, J.S. Smith, V.B. Prakapenka, T. Katsura, N. Dubrovinskaia, A.F. Goncharov and L. Dubrovinsky, *Chem. Mater*., 2022, **34**, 8138−8152.

65. Y. Pan, Y. Lin and C. Tong, *J. Phys. Chem. C*, 2016, **120**, 21762−21769.

66. A. Ivanovskii, *Prog. Mater. Sci.*, 2012, **57**, 184−228.

67. C. Wang and L. Song, *Can. J. Phys*., 2017, **95**, 621–624.

68. S. Otani, M. M. Korsukova and T. Aizawa, *J. Alloys Comp*., 2009, **477 (1–2)**, L28-L29.

69. W. Zhou, H. Wu and T. Yildirim, *Phys. Rev. B*, 2007, **76**, 184113.

70. J. B. Levine, J. B. Betts, J. D. Garrett, S. Q. Guo, J. T. Eng, A. Migliori and R.B. Kaner, *Acta Mater.*, 2010, **58(5)**, 1530-1535.

DATA AVAILABILITY STATEMENTS

Crystal structure, bonding and electronic structure
of α- and β-Ir_2B_{3-x} compounds

Oksana Sologub[1,*], Leonid P. Salamakha[1,5], Berthold Stöger[2], Takao Mori[3],
Neven Barisic[1,6], Peter F. Rogl[4], Herwig Michor[1], Ernst Bauer[1]

1. Crystallographic data for α-Ir_2B_{3-x} have been deposited at the CCDC under the deposition number 2371295.

2. The data supporting this article have been included as part of the Supplementary Information. The Supporting Information includes: Powder X-ray diffraction pattern of ~$Ir_{50}B_{50}$ (in at. %) sample obtained from high-temperature synthesis and crystallographic characteristics of the phases elucidated from Rietveld refinement; Partial electron densities of states of individual atoms in α-Ir_2B_{3-x} and β-Ir_2B_{3-x} structures calculated with and without SOC; Sections of calculated electron localization function in α-Ir_2B_{3-x} and β-Ir_2B_{3-x} visualizing boron-iridium bonding; Unit cells of a series of boride structures exhibiting chair-like configuration of boron hexagons in comparison with α-Ir_2B_{3-x}.